

https://dspace.org/

Laser powder bed fusion of Ti6Ta15Zr02Ru5Cu mass process parameter evaluation using single tracks analysis

N Phala; Claudia Polese; J Ciftci; Lesley Cornish

https://hdl.handle.net/10539/43612
DOAJ

Downloaded from a DSpace repository. https://dspace.org/

Laser powder bed fusion of Ti-6Ta-1.5Zr-0.2Ru-5Cu (mass%) – process parameter evaluation using single tracks analysis

Ngwakoana Phala[1*], *Claudia* Polese[2], *Jakub* Ciftci[3,4], *Tomasz* Choma[3,4], and *Lesley* Cornish[1]

[1]School of Chemical and Metallurgical Engineering and DSI-NRF CoE in Strong Materials, University of the Witwatersrand, Johannesburg, South Africa
[2]School of Mechanical, Aeronautical and Industrial Engineering, University of the Witwatersrand, Johannesburg, South Africa
[3]Warsaw University of Technology, Faculty of Materials Science and Engineering, Wołoska 141, 02-507 Warsaw, Poland
[4]AMAZEMET Sp. z o. o. [Ltd.], Al. Jana Pawła II 27, 00-867 Warsaw, Poland

Abstract. Printing of single tracks from atomised powder was carried out to determine the potential parameters for Laser Powder Bed Fusion of Ti-6Ta-1.5Zr-0.2Ru-5Cu (mass%). Parameters that were varied included laser power, scanning speed, beam diameter, linear and planar energy density. The single tracks were characterised by SEM and SEM-EDX, showing variations in microstructural homogeneity. Promising tracks were produced using laser power of 157.5 W, scanning speed of 600 mm/s, beam diameter of 0.15 mm, 0.263 J/mm linear energy and 1.750 J/mm^2 planar energy density. XRD for one of these tracks indicated (αTi) and (βTi) solid solutions as well as the Ti_2Cu phase.

1 Introduction

Laser Powder Bed Fusion (LPBF) is an additive manufacturing (AM) technique that involves applying thin layers of powder to a build plate and using a laser energy source, fuses the powder based on the designed geometry [1]. Powders are heated and fused layer-by-layer according to the design created in computer-aided design (CAD) software to produce near-net-shapes [2]. This can be done to build Ti-based alloy components with complicated

* Corresponding author: 820850@students.wits.ac.za

© The Authors, published by EDP Sciences. This is an open access article distributed under the terms of the Creative Commons Attribution License 4.0 (https://creativecommons.org/licenses/by/4.0/).

geometries and excellent mechanical properties [2], which is beneficial for increased design flexibility for complex geometries, shorter production times and less material waste [3].

LPBF is now being used to produce near full density (99.5%) parts with mechanical properties like those fabricated using conventional methods although they are still weaker when exposed to cyclic loading [1]. Medical devices are a significant portion of the AM market, and the request for healthcare components is increasing for therapeutic delivery, surgical planning, implant design and tissue engineering applications [4]. AM can be used to customise medical devices and prostheses to the unique anatomy of each patient [5].

Titanium alloys are used in dental implants because of their excellent properties, including biocompatibility, osseointegration and good mechanical properties [6]. Ti-6Ta-1.5Zr-0.2Ru-5Cu (mass%) was developed as a potential α+β alloy for biomedical implants [7]. The addition of 5 mass% copper promotes good antibacterial properties thanks to the formation of Ti_2Cu precipitates [6], as well as balanced mechanical properties. A 0.2 mass% ruthenium addition enhanced corrosion resistance without changing the microstructure [7]. In dental implants, corrosion resistance is important as mouths have various electrolytes with some corrosive species. The as-cast Ti-6Ta-1.5Zr-0.2Ru-5Cu (mass%) alloy [7] had the required Ti_2Cu precipitates, Fig. **1**. Spherical atomised powder of the same composition had been produced with particle sizes within a 10-100 µm range for compatibility with the LPBF process [8].

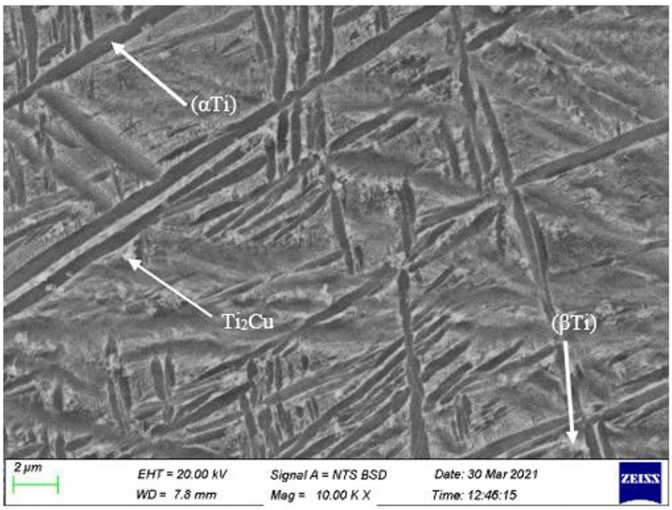


Fig. 1. SEM-BSE image of as-cast Ti-6Ta-1.5Zr-0.2Ru-5Cu (mass%) showing inside one grain with (αTi) needles (dark), (βTi) matrix (medium) and Ti_2Cu (light) [7].

To achieve the desired properties, optimisation of LPBF process parameters is necessary to produce high-quality, defect-free components [9]. Thus, it is important to understand the relationship between the processing parameters, geometry and the resulting microstructure [10]. Preliminary methods that are mostly used are expensive and require more material and energy, as aviation standards mention that the first 2.5 mm of the part from the base plate should be discarded as the process has not reached thermal stability [11]. A more recent single track approach is instead cost-effective as it requires less material and

energy to preliminarily evaluate the effects of different combinations of LPBF process parameters on the geometric characteristics of the obtained deposit and the changes in microstructure [12]. While these single tracks might primarily indicate weldability, as the interaction with the base plate limits their ability to provide insights into the final properties of the components, they can help identify a suitable process window to build complex 3D shapes.

In LPBF, the influence of laser power and scan speed on AM components is important [12]. Linear energy density (LED), defined as the ratio of laser power to scan speed, significantly impacts the melt pool's characteristics, including its shape and thermal dynamics, which in turn affect the microstructure, grain size, porosity and mechanical properties of the final part [13]. Additionally, factors such as the base plate size and powder characteristics influence cooling rates, ultimately determining microstructure and mechanical properties. Utilising a finer laser spot size can create a localised concentration of heat, yielding more energy for a given laser power and scan speed. Moreover, planar energy density (PED), which is the energy input per unit area, along with the thermal properties of the powder, offers a deeper understanding of the melting and fusing processes [12]. Controlling PED is crucial for achieving the desired dimensional and morphological characteristics of the melt pool, ensuring good adhesion between the base substrate and the fused tracks [12].

This study investigates LPBF of a newly developed Ti-6Ta-1.5Zr-0.2Ru-5Cu (mass%) alloy, aiming to identify potential process parameters through single tracks analysis. Single tracks printing experiments were performed with varying laser power, scanning speed and beam diameter. The analysis of the surface of the LPBF single tracks involved their morphology and microstructural characterisation, in comparison to the as-cast alloy, using SEM, EDX and XRD. The final goal is to fabricate defect-free components for biomedical implants using a newly developed Ti-Cu alloy with improved antibacterial properties, contributing to the expansion of the LPBF process in the field.

2 Experimental procedure

Single tracks of atomised powder of Ti-6Ta-1.5Zr-0.2Ru-5Cu (mass%) [8] were printed using an AconityMIDI system with different parameters, Table 1. The particle size used was 30-60 µm. The single tracks were LPBF printed on squares made of 20 layers of this alloy on a 1 mm thick disc of Ti-6Al-4V used as the substrate, see Figure 2. This was done to prevent melting of the substrate and prevent the influence of its chemical composition on the single tracks. Subgroups of five single tracks, each with a different parameter combination, as reported in A LPBF sample was prepared using standard metallographic preparation and polished using colloidal silica.

Table *2*, were printed on eight supporting squares. Fig. ***2*** shows also the directions of argon gas for oxidation prevention, melting and recoating (the blade that is used to coat a layer of powder during LPBF).

Table 1. Printing range parameters for the single tracks.

Laser power	**Scanning speed**	**Beam diameter**	**Linear energy density**	**Planar energy density**
120-280 W	200-1200 mm/s	0.08-0.36 mm	0.120-0.7880 J/mm	0.600-9.844 J/mm^2

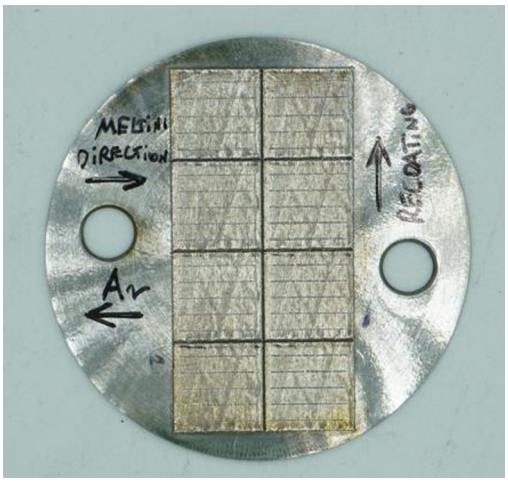


Fig. 2. Photograph of the Ti-6Al-4V substrate disc with 8 LPBF squares supporting 5 horizontal single tracks each, showing directions of argon gas flow, melting and recoating.

Micrographs of the tracks from different processing parameters were compared using scanning electron microscopy (SEM) (Zeiss Sigma Field Emission Scanning Electron Microscope (FEG-SEM500)) to check if they were printed evenly. The compositions were analysed using energy dispersive X-ray spectroscopy (EDX) on the SEM to ascertain whether they were homogeneous and of the targeted composition. The squares with the single tracks were removed from the disk using electrical discharge machining (EDM). An X-ray diffraction (XRD) D2 Phaser (Bruker XRD) with Co-Kα radiation (λ=1.78899 Å) was operated at 50 kV and 20 mA with a nickel filter, scanning for 10-130° degrees for 17 minutes to identify the phases. A LPBF sample was prepared using standard metallographic preparation and polished using colloidal silica.

Table 2. Printing parameters for the single tracks.

Number	Laser power (W)	Scanning speed (mm/s)	Beam diameter (mm)	Linear energy density (J/mm)	Planar energy density (J/mm^2)
1.	171	600	0,08	0,285	3,563
	171	400	0,08	0,428	5,344
	171	600	0,15	0,285	1,900
	171	400	0,15	0,428	2,850
	171	200	0,15	0,855	5,700
2.	157.5	1200	0,08	0,131	1,641
	157.5	1000	0,08	0,158	1,969
	157.5	800	0,08	0,197	2,461
	157.5	600	0,08	0,263	3,281
	157.5	400	0,08	0,394	4,922
3.	157.5	1200	0,15	0,131	0,875
	157.5	1000	0,15	0,158	1,050
	157.5	800	0,15	0,197	1,313
	157.5	600	0,15	0,263	1,750
	157.5	400	0,15	0,394	2,625
4.	157.5	600	0,22	0,263	1,193
	157.5	600	0,15	0,263	1,750
	157.5	600	0,08	0,263	3,281
	120	1000	0,15	0,120	0,800
	120	1000	0,08	0,120	1,500
5.	315	1200	0,08	0,263	3,281
	315	1000	0,08	0,315	3,938
	315	800	0,08	0,394	4,922
	315	600	0,08	0,525	6,563
	315	400	0,08	0,788	9,844
6.	315	1200	0,15	0,263	1,750
	315	1000	0,15	0,315	2,100
	315	800	0,15	0,394	2,625
	315	600	0,15	0,525	3,500
	315	400	0,15	0,788	5,250
7.	157.5	600	0,36	0,263	0,729
	157.5	600	0,29	0,263	0,905
	157.5	600	0,22	0,263	1,193
	157.5	600	0,15	0,263	1,750
	1575	600	0,08	0,263	3,281
8.	280	1200	0,36	0,233	0,648
	280	1200	0,29	0,233	0,805
	280	1200	0,22	0,233	1,061
	280	1200	0,15	0,233	1,556
	280	1200	0,08	0,233	2,917

3 Results and discussion

Figure 3 shows the morphology of the single tracks of Ti-6Ta-1.5Zr-0.2Ru-5Cu (mass%) for constant laser power and beam diameter, with varying scanning speeds. The un-melted spherical particles in Figure 3a had a particle size of 51.4±1.9 µm which was within the 45-60 µm average particle size of the atomised powder [8]. The un-melted spherical powders were randomly distributed and were present in all the samples; some samples had more un-melted spherical particles, Figure 3a, and others had fewer, Figure 3c. Figure 3d shows that at higher scanning velocities, the tracks were unstable along the printing direction, and "balling" occurred as shown by the circle. Balling is a surface defect that occurs because of severe instability of the molten pool induced by the high melt viscosity under a relatively low energy density [12], decreasing surface quality and densification [13]. Gao et al. [16] demonstrated that large Marangoni convection and liquid capillary instability in the molten pool were the primary causes of balling at high scanning speed. Balling, shown in Figure 3d, is caused by insufficient contact of the melt with the solid substrate and occurs at high scanning speeds due to the limited energy input [17]. The dark particles in Figure 3d were contaminations from separating different squares of tracks using EDM.

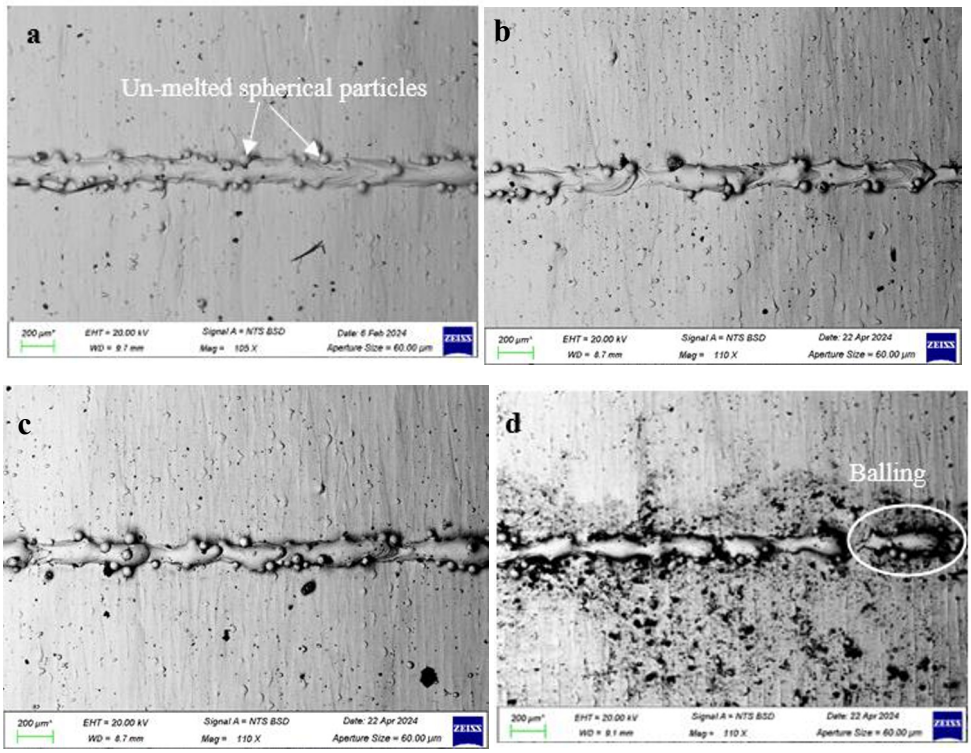


Fig. 3. SEM-BSE images show the morphology of the single tracks at constant laser power: 157.5 W, beam diameter: 0.15 mm and scanning speeds of (a) 600 mm/s, (b) 800 mm/s, (c) 1000 mm/s and (d) 1200 mm/s, the white circle showing the balling.

Fig. ***4*** shows that increasing the laser powder and reducing the beam diameter reduced "balling" at higher scanning speeds. High voltage and lower scanning speed results in higher

LED which causes porosity [12]. However, Fig. ***4***d shows that high scanning speed results in balling**.** Guo et al. [18] studied single-track fabrication of niobium and titanium alloys finding that when laser energy density increased, the track width and substrate penetration also increased. This was found in this work because when the LED increased, the tracks were more even.

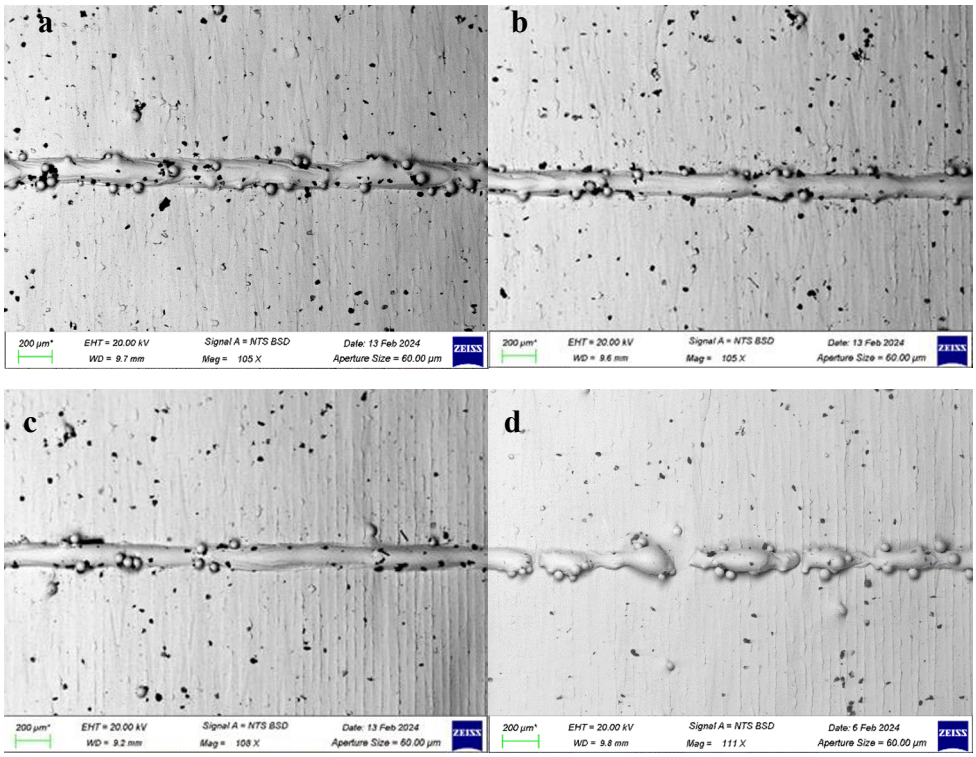
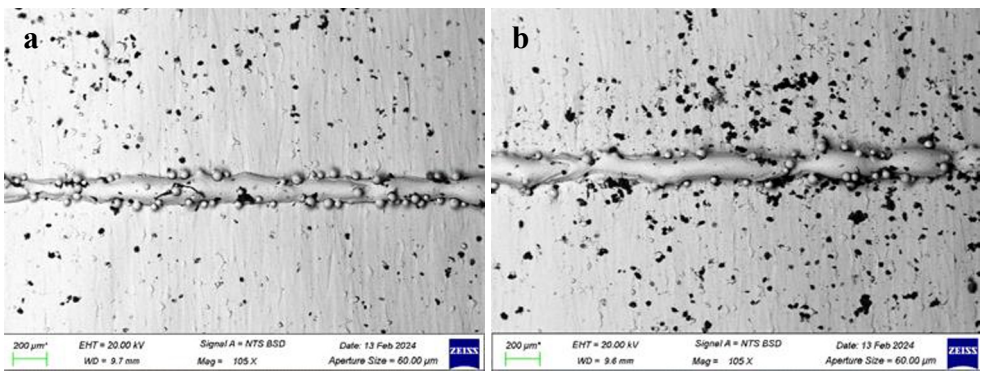


Fig. 4. SEM-BSE images showing the morphology of single tracks at 315 W laser power, 0.08 mm beam diameter and scanning speeds of: (a) 600 mm/s, (b) 800 mm/s, (c) 1000 mm/s and (d) 1200 mm/s.

Fig. ***5*** shows that "balling" at higher voltage and higher scanning speed increased with increasing beam diameter. High beam diameter resulted in lower PED which caused rougher surfaces and lower hardness [19], and Fig. ***5***c and 5d show that lower PED caused balling.



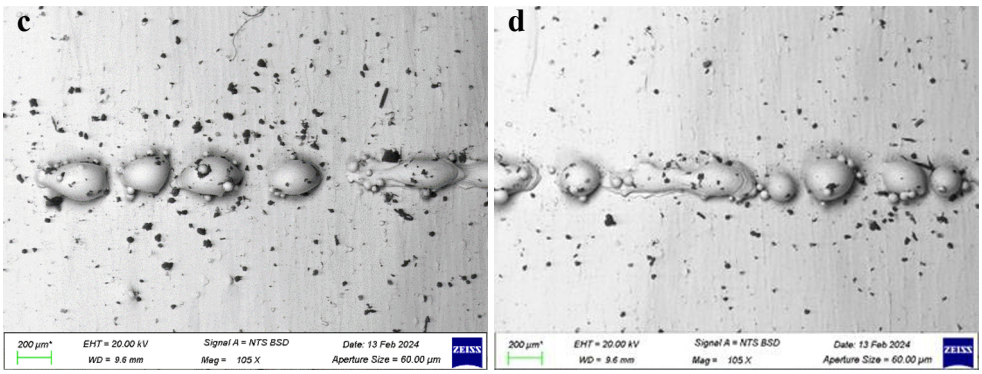


Fig. 5. SEM-BSE images showing the morphology of the single tracks at 280 W constant laser power and 1200 mm/s scanning speed for beam diameter: (a) 0.15 mm, (b) 0.22 mm, (c) 0.29 mm and (d) 0.3 mm.

Fig. ***3***a identified the best single track which was even, continuous with a smooth surface. Although the tracks in Fig. ***4***a-c also appear good, they were done with high LED which can cause porosity [12], even though no porosity was observed on any single track surface (and the surfaces were not sectioned)**.** "Balling" is undesirable in LPBF because it can lead to inhomogeneity in the next powder layer or to collisions with the recoater/roller that deposits the powder layer [19]. The best single track was printed using 157.5 W laser power, 600 mm/s scanning speed, 0.15 mm beam diameter, 0.263 J/mm linear energy and 1.750 J/mm^2 planer energy density, so these were identified as potential parameters.

Fig. ***6*** shows a higher magnification image of the best single track within the analysed combinations showing nucleation sites with the dendrites growing out from them.

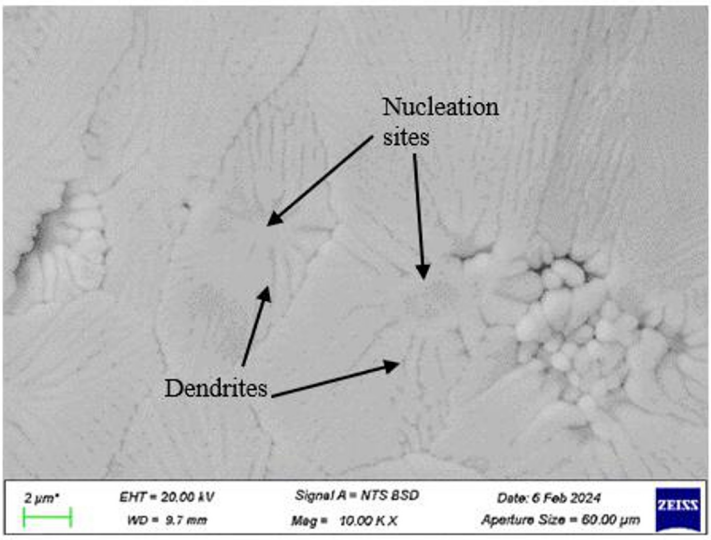


Fig. 6. SEM-BSE image showing the best single track of Ti-6Ta-1.5Zr-0.2Ru-5Cu (mass%) at higher magnification.

Fig. *7* shows the microstructure of the LPBF sample. The previous as-cast sample [7], Figure 1, had (βTi) needles, while the LPBF microstructure showed (αTi) formed along the grain boundaries with small precipitates in the (βTi) matrix. The difference in the microstructures was due to the different solidification rates.

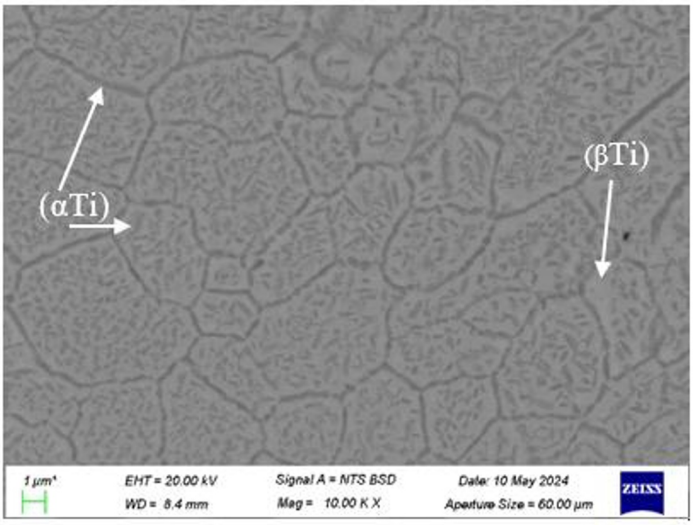


Fig. 7. SEM-BSE image of LPBF Ti-6Ta-1.5Zr-0.2Ru-5Cu (mass%), showing inside (αTi) along grain boundaries and dendrites within (βTi).

The expected composition was obtained for the spherical particle and the best single track, as shown in Table 3. The EDX results were the same for Ta and Ru, The LPBF sample had slightly higher Cu and lower Ti and Zr than the as-cast sample [7]. The dark spot was mostly contamination,
Table *4*.

Table 3. EDX results from as-cast [7], surface of the best single track and the spherical particle of Ti-6Ta-1.5Zr-0.2Ru-5Cu (mass%).

Alloy	EDX (mass%)				
	Ti	Ta	Zr	Ru	Cu
As-cast [7]	86.0±1.6	7.4±0.9	2.0±0.8	0.4±0.6	4.5±1.5
Best single track	83.8±1.5	7.4±0.3	1.7±0.1	0.4±0.1	6.7±1.8
Spherical Particles	81.6±1.5	7.4±0.2	1.9±1.5	0.2±0.1	8.9±0.1

Table 4. EDX result of dark spot on Ti-6Ta-1.5Zr-0.2Ru-5Cu (mass%) best single track.

Alloy	C	O	Si	Cl	K	Ti	Fe

Dark spot	42.6±5.6	34±9.4	0.7±0.1	0.6±0.4	3,2±1.4	18±2.8	0.9±0.1

Fig. ***8*** shows the XRD pattern of the best single track of Ti-6Ta-1.5Zr-0.2Ru-5Cu (mass%) identifying (αTi), (βTi) and the Ti_2Cu phase which is beneficial for enhancing the antibacterial properties of the alloys [6]. Although Canale and Servant [21] identified Ti_3Cu on solidification and Fowler [22] identified it in a 5 mass% Cu sample, the XRD peaks are so similar to Ti_2Cu that they are indistinguishable at low amounts and Ti_3Cu is not stable [23]. Tantalum, zirconium and ruthenium were not detected, because they were dissolved in the (αTi) and (βTi) solid solutions.

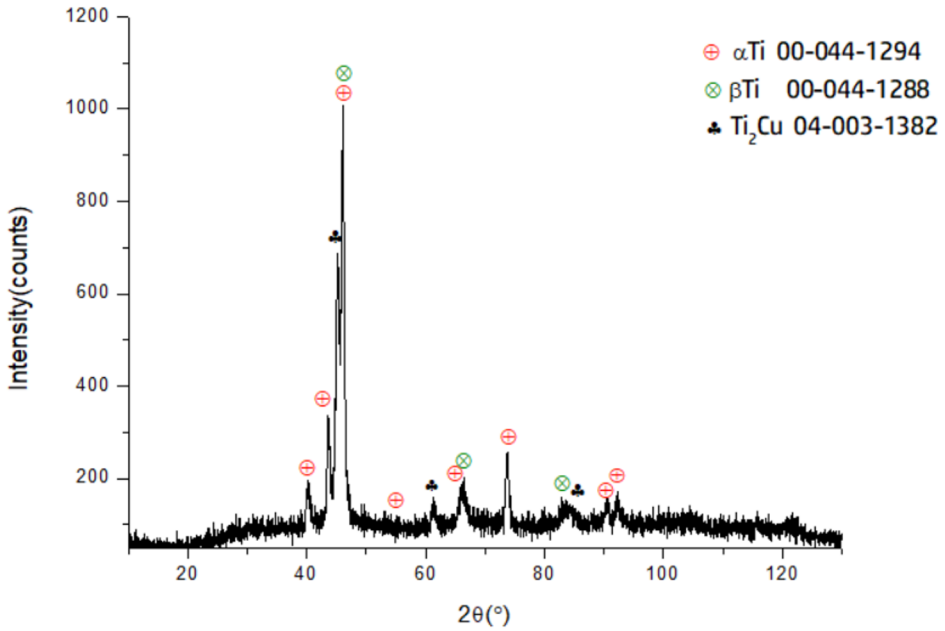


Fig. 8. XRD pattern of the best single track of Ti-6Ta-1.5Zr-0.2Ru-5Cu (mass%).

4. Conclusions

The best LPBF Ti-6Ta-1.5Zr-0.2Ru-5Cu alloy (mass%) tracks produced during this preliminary study were even, smooth and continuous, with the targeted alloy composition. The parameters for these tracks were 157.5 W laser power, 600 mm/s scanning speed, 0.15 mm beam diameter, 0.263 J/mm linear energy and 1.750 J/mm² planar energy density. Their surface microstructure consisted of a matrix of βTi, with αTi located at the grain boundaries and precipitated within the grains. These LPBF tracks exhibited smaller grains compared to the as-cast sample. X-ray diffraction (XRD) analysis of the surface of these LPBF tracks identified the presence of αTi, βTi, and Ti_2Cu phases.

The authors would like to acknowledge National Research Foundation, DSI-NRF CoE in Strong Materials (Grant UID 41292) and the Collaborative Programme on Additive Manufacturing (CPAM) (Contract CSIR-NLC-CPAM-21-MOA-WITS-01) for financial support, Warsaw University of Technology and AMAZEMET for printing single tracks, Letta Ntuli for XRD analysis, and Collen Makola for SEM analysis.

References

1. W.E. King, A.T. Anderson, R.M. Ferencz, N.E. Hodge, C. Kamath, S.A. Khairallah, and A.M. Rubenchik. Laser powder bed fusion additive manufacturing of metals; physics, computational, and materials challenges. App Phy Rev, **2**(4), pp 1-27, (2015).
2. H.L. Wei, Y. Cao, W.H. Liao, and T.T Liu 2020. Mechanisms on inter-track void formation and phase transformation during laser powder bed fusion of Ti-6Al-4V. *Add Man*, **34**, pp.101221-101237, (2020).
3. K. Raut, A.K Ball, and A. Basak, A. Impact of track length, track shape, and track location on thermal distortion in laser powder bed fusion of IN625: Single laser vs. three lasers. J of Eng Res, pp 1-16, (2023).
4. T. Nakano and T. Ishimoto. Powder-based additive manufacturing for development of tailor-made implants for orthopedic applications. *KONA Powder and Particle Journal*, **32**, pp.75-84, (2015).
5. A. Nouri, A.R. Shirvan, Y. Li, and C. Wen, C. Additive manufacturing of metallic and polymeric load-bearing biomaterials using laser powder bed fusion: A review. J of Mat Sci & Tech, **94**, pp.196-215, (2021).
6. E. Zhang, F. Li, H. Wang, J. Liu, C. Wang, M. Li, K. Yang. A new antibacterial titanium–copper sintered alloy: preparation and antibacterial property. Mat. Sci. Eng. C, **33** (7), pp. 4280-4287, (2013).
7. L. Spotose. Identifying Ti-Cu-based alloys for biomedical applications, MSc dissertation, University of the Witwatersrand, (2023).
8. N.S. Phala, C. Polese, T. Choma, H. Möller, Ł. Żrodowski, and L.A.Cornish. Atomisation of Ti-6Ta-1.5 Zr-0.2 Ru-5Cu (wt%) for additive manufacturing for biomedical applications. In *MATEC Web of Conferences* (Vol. 388, p. 08003). EDP Sciences, (2023).
9. A. Carrozza, F. Mazzucato, A. Aversa, M. Lombardi, F Bondioli, S. Biamino, A. Valente, and P. Fino. Single scans of Ti-6Al-4V by directed energy deposition: a cost and time effective methodology to assess the proper process window. Met and Mat Int, pp.1-13, (2021).
10. D. Svetlizky, B. Zheng, D.M. Steinberg, J.M. Schoenung,E.J. Lavernia, and N. Eliaz. The influence of laser directed energy deposition (DED) processing parameters for Al5083 studied by central composite design. J of Mat Res and Tech, **17**, pp.3157-3171, (2022).

11. B. Blakey-Milner, P. Gradl, G. Snedden, M. Brooks, J. Pitot, E. Lopez, M.F. Leary,. Berto and A. Du Plessis . Metal additive manufacturing in aerospace: A review. *Mat & Des*, *209*, pp.110008-110048, (2021).

12. A. Gonnabattula, R.S. Thanumoorthy, S. Bontha, A.A.S. Balan, V.A. Kumar, and A.K. Kanjarla. Process parameter optimization for laser directed energy deposition (LDED) of Ti6Al4V using single-track experiments with small laser spot size. Optics & Laser Tech, **175**, pp.110861-110873, (2024).

13. D.D. Gu, W. Meiners, K. Wissenbach, and R. Poprawe. Laser additive manufacturing of metallic components: materials, processes and mechanisms. Int Mat Rev, **57**(3), pp.133-164, (2012).

14. D. Dai, D. Gu, Q. Ge, Y. Li, X. Shi, Y. Sun, and S. Li, S., 2020. Mesoscopic study of thermal behaviour, fluid dynamics and surface morphology during selective laser melting of Ti-based composites. Comp Mat Sci, **177**, pp.109598-109609, (2020).

15. J Sun, M. Guo, K. Shi, and D. Gu. Influence of powder morphology on laser absorption behaviour and printability of nanoparticle-coated 90W-Ni-Fe powder during laser powder bed fusion. Mat Sci in Add Man, **1**(2), pp.11-24, (2022).

16. P. Gao, Z. Wang, and X. Zeng. Effect of process parameters on morphology, sectional characteristics and crack sensitivity of Ti-40Al-9V-0.5 Y alloy single tracks produced by selective laser melting. Int J of Light Mat and Man, **2**(4), pp.355-361, (2019).

17. J. Robinson, M. Stanford, and A. Arjunan. Stable formation of powder bed laser fused 99.9% silver. Mat Today Com, **24**, pp.101195-101208, (2020).

18. Y. Guo, J.I.A. Lina, B Kong, N.A. Wang, and H. Zhang. Single track and single layer formation in selective laser melting of niobium solid solution alloy. Chin J of Aer, **31**(4), pp.860-866, (2018).

19. Y. Liu, J. Li, K. Xu, T. Cheng, D. Zhao, W. Li, Q. Teng, and Q. Wei, Q., 2022. An optimized scanning strategy to mitigate excessive heat accumulation caused by short scanning lines in laser powder bed fusion process. Add Man, **60**, pp.103256-103268, (2022).

20. I. Yadroitsev, and I. Yadroitsava. A step-by-step guide to the L-PBF process. In Fundamentals of laser powder bed fusion of *metals* (pp. 39-77). Elsevier, (2021).

21. P. Canale and C. Servant. Thermodynamic assessment of the Cu–Ti system taking into account the new stable phase $CuTi_3$. Inter J of Mat Res, **93**(4), pp.273-276, (2022).

22. L. Fowler. Development of titanium-copper alloys for dental applications (Doctoral dissertation, Acta Universitatis Uppsaliensis), (2019).

23. K. Dyal Ukabhai, U.A Curle, N.D.E. Masia, M. Smit, I.A. Mwamba, S. Norgren, C. Öhman-Mägi, N.G. Hashe, and L.A. Cornish. Formation of Ti_2Cu in Ti-Cu alloys, J. Phase Equil and Dif, **43**, pp. 332-344, (2022).